Ni composite electrodes for hydrogen generation: Activation of Nb-based semiconductors

Esteban A. Franceschini [a,b,**], Victoria Benavente Llorente [b], Anabel E. Lanterna [a,c,*]

[a] Department of Chemistry and Biomolecular Sciences, Centre for Advanced Materials Research (CAMaR), University of Ottawa, Ottawa, Canada
[b] INFIQC, CONICET, Departamento de Fisico-Quimica, Facultad de Ciencias Quimicas, Universidad Nacional de Córdoba, Córdoba, Argentina
[c] School of Chemistry, University of Nottingham, University Park, Nottingham, NG7 2RD, UK

HIGHLIGHTS

- Small amounts of Co or Cu species greatly affect Nb-based Ni composite electrodes activity.
- Similar Cu loadings suggest electrode enhanced activity depends on the semiconductor.
- Cu oxides-Nb phosphate heterojunction shows the highest catalytic activity.
- Cu species induce slight photoelectrochemical effects.

GRAPHICAL ABSTRACT
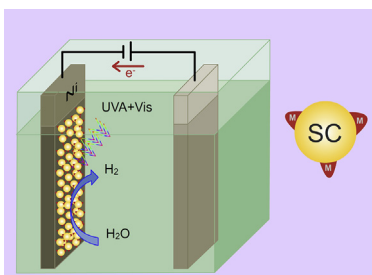
ABSTRACT

The hydrogen evolution reaction depends on the accumulation of electrons on the catalytic center to enable the two-electron processes involved in water reduction. This work reports on the modification of inexpensive nickel (Ni) composite electrodes with engineered semiconductor heterojunctions based on earth-abundant transition metals that show superior hydrogen generation activity in the presence of a non-toxic electrolyte (K_2CO_3). This is, small amounts of cobalt (Co) or copper (Cu) oxides can improve the reactivity of composite electrodes formed by deposition of titanium (Ti) or niobium (Nb) semiconductors onto Ni surfaces. In general, modified Nb-based semiconductors show better performance and their enhanced activity can be understood in terms of modified surface potentials upon formation of semiconductor-Ni heterojunctions. Photoelectrochemical activity can be detected in the presence of Cu oxides, where hydrogen generation onset potential is reduced under UV–Vis light irradiation. The study demonstrates that small composition

changes can greatly affect the activity of Nb-based Ni composite electrodes, showing exciting new applications for Nb-based materials.

Introduction

The use of hydrogen as an alternative to fossil fuels has gained attention as a way to eliminate the emission of greenhouse gases during combustion. However, current industrial production of hydrogen relies on the use of natural gas generating significant carbon emissions. Since the first report on the photoelectrochemical generation of hydrogen from water [1], many efforts have been focused on the production of "clean" hydrogen using renewable energy sources with zero net carbon emissions. Nevertheless, the price of the green electricity used in the electrolysis process is still high to allow for technology transfer [2–4]. Therefore, the development of inexpensive electrocatalytic systems with high hydrogen generation efficiency is of paramount importance to develop a sustainable future that can rely on the use of solar energy storage to supply the global energy demands.

The design of electrodes that can improve the hydrogen production whereas using earth-abundant and inexpensive materials can contribute to the advance of H_2 technologies in real applications [5]. In this regard, alkaline electrolizers using Ni electrodes are an appealing method for large-scale production of H_2 [6–11]. Ni electrodes usually present low catalytic activity and fast deactivation processes that generate unreactive surface species (hydrides, hydroxides, and other oxygenated species [12,13]). However, modification of the Ni surface can extend the electrode lifetime, thereby improving the efficiency of the hydrogen evolution reaction (HER). For instance, we have recently shown that the modification of Ni electrodes with n-type semiconductors (SC) such as TiO_2 and Nb_2O_5, using Nafion as a binder, can improve the electron flux into Ni electrocathodes under dark [14,15] or under photochemical conditions [16]. One of the advantages of using semiconductors to modify the electrochemical behaviour of electrodes is their perceived ability to form rectifying junctions by simple structural modifications [17–21]. Different semiconductor heterojunctions can be engineered [22,23] to lower the Schottky barrier formed with the Ni electrode [24]. Based on Schottky's theory, the inclusion of a third metal such as cobalt (Co) or copper (Cu) could generate an electron flow that improves even further the interaction between nickel and the oxides, and that could improve the catalytic activity of the SC-Ni electrodes [25–27]. Additionally, the use of multiple band gap electrodes to capture a greater fraction of the solar light has also motivated to engineer multi-electron accumulation systems [28–31]. Such systems can benefit from the unidirectional electron flow that accumulates charges on the catalytic sites, favouring the two-electron reaction that generates H_2 from water.

Here we show that simple modification of semiconductor heterostructures with earth abundant metals (M@SC) can enhance Ni electrodes efficiency up to 3 orders of magnitude when comparing to electrodes modified with the bare semiconductor (SC–Ni). In particular, we have used copper or cobalt oxides to decorate the surface of transition metal semiconductor —i.e., TiO_2, Nb_2O_5, and $Nb_3(PO_4)_5$—which have previously shown enhanced activity towards HER under alkaline conditions using Ni electrodes [14,15].

Experimental

Materials and instruments

Ni plates (99.99%) were purchased from Cordes SA Argentina. Nafion and 2-propanol were purchased from Sigma and used as received. DI H_2O was obtained by purification of deionized water using a Thermo Scientific™Barnstead™GenPure™water purification system (conductivity = 18.2 MΩ-cm) and TiO_2 P25 was purchased from Univar Canada. Niobium oxide (Nb_2O_5) and niobium phosphate ($Nb_3(PO_4)_5$) were generously provided by CBMM (Companhia Brasileira de Metalurgia e Mineração) and used as received. $CuCl_2 \cdot 2H_2O$ and $Co(NO_3)_2 \cdot 6H_2O$ were obtained from Aldrich, I-2959 from BASF and I-907 from CIBA-GEIGY.

X-ray powder diffraction (XRD) patterns were recorded on a PANalytical X'Pert PRO diffractometer operating at 40 kV and 40 mA using $\lambda = 1.5406$ Å Cu Kα radiation employing in the θ-2θ Bragg-Brentano geometry. All measurements were carried out at room temperature. The 2θ range used was 10–90°, with 0.02° steps and counting time of 5 s per step. The Rietveld method was used to refine the crystal structure employing the FullProf program [32]. A pseudo-Voigt shape function was used to fit the experimental data. The data refined were lattice parameters, atomic positions, isotropic thermal parameters, peak shape, and occupation factors.

Raman spectra of the electrode surface were acquired with a LABRAM-HR 800, HORIBA Jobin-Yvon Raman microscope with a 100× objective lens (NA = 0.9). The laser excitation used was 632.8 nm at 3.5 mW. The instrument allows recording spectra with a resolution of 1.5 cm^{-1}. The illuminated area in all Raman experiments was 1.0 μm^2. At least five different zones on each sample were analyzed to confirm the homogeneity of the catalysts.

AIST-NT Scanning Probe Microscope (SPM) SmartSPM-1000 was utilized to record topography and non-contact potential measurements using Au-coated tips purchased from Mikro-Masch with a radius < 35 nm, a stiffness of 1.8–13 N m^{-1}, and a resonant frequency of 110–220 kHz. All measurements were performed in non-contact AFM mode and single pass Kelvin Probe Force Microscopy (KPFM) in the dark or under visible light irradiation. The 5 × 5 μm area of study was scanned at 1 μm s^{-1}. For each scan line, the height profile was recorded in

the first pass and then the tip was lifted 10 nm away from the surface and the potential offset was measured.

Scanning electron microscopy (SEM) images were obtained using a JEOL JSM-1600 SE microscope working at an accelerating voltage of 2 kV.

Electrochemical measurements were carried out using the Parstat 2273 advanced electrochemical system in a conventional three-electrode electrochemical cell. A Pt wire was used as counter electrode and saturated calomel electrode (SCE) as reference electrode (0.243 V vs. RHE).

Synthesis of semiconductor heterostructures

The preparation of the SC heterostrucutres used in this work (denoted as M@SC) was performed using a reported methodology [33,34]. Briefly, Cu@SC heterostrucutres were prepared by mixing 21.2 mg of $CuCl_2 \cdot 2H_2O$ with 160 mg of the corresponding SC and 56 mg of Irgacure-2959 (I-2959) in 100 mL of DI Water. The mixture was purged with argon, sonicated for 15 min and irradiated for 5 h under UVA light (Fig. S1). The resulting slurry was filtered through nanopore filter and dried overnight under vacuum. Similarly, Co@SC heterostructures were obtained using 41.6 mg of $Co(NO_3)_2 \cdot 6H_2O$, 160 mg of SC and 78 mg of I-907 mixed together in 150 mL of dry acetonitrile. The mass of the Cu and Co precursors were selected to keep the number of moles of the metals constant during the synthesis. Metal loading was determined by Inductively Coupled Plasma Optical Emission Spectroscopy (ICP-OES), using an Agilent Vista Pro ICP Emission Spectrometer. Samples (10 mg) were prepared in triplicates by digestion in aqua regia. Further dilutions were prepared and analysed following the Cu 324.754 nm emission line.

Electrodes preparation

The nickel supports were prepared as previously reported [14]. Initially they were degreased with acetone, and before applying the catalyst the supports were peeled by successively immersing them in 15% HCl and 1 M KOH for 1 min. The electrodes were prepared by drop casting method [35,36]. Briefly, 5 mg of catalyst were dispersed in 30 mg of DI H_2O, 300 mg of 2-propanol and 15 mg of 5 wt% Nafion solution; and sonicated for 30 min. Then, 350 μL of the Nafion-based ink were pipetted onto a polished (#600 sandpaper) square-shaped Ni electrode (1 cm^2) and air-dried at 60 °C temperature.

Electrochemical measurements

The (photo)electrochemical generation of hydrogen and the electrochemical characterization − cyclic voltammetry (CV), open-circuit potential (OCP), and electrochemical impedance spectroscopy (EIS) − of the electrodes was carried out in a conventional three-electrodes electrochemical cell using a home-made photoreactor previously described [14] (See Fig. S2) with a 0.5 M K_2CO_3 solution (pH = 11). The electrolyte was chosen as a non-toxic alternative to common NaOH or KOH. All solutions were prepared in Milli-Q water and deoxygenated by bubbling high purity nitrogen. Temperature inside the electrochemical cell was kept at 298 K (±2 °C).

Open circuit potential (OCP)

Open circuit potential measurements were performed using a pre-built method consisting on applying a close-to-zero current density and measuring the transient potential with time. The OCP experiments were performed in the dark and under a combination of UVA and Vis light irradiation (Fig. S3).

Electrochemical impedance spectroscopy (EIS)

EIS experiments were carried out using a frequency range between 10 mHz and 200 kHz with a 10 mV bias potential at different electrode potentials. The potentials selected corresponds with Ni open-circuit potential (OCP, −0.36 V vs SCE), HER onset potential (OP) over pure Ni (−1.1 V vs SCE), −1.2 V vs. SCE, and −1.4 V vs. SCE in order to cover the potential range where the HER occurs [37,38]. The ZView 3.3 software (Scribner Associates, Inc.) was used to fit the measured data with different equivalent circuit models.

Results and discussion

Characterization of M@SC-Ni electrodes

Ni electrodes were modified using different metal-semiconductor heterostructures denoted as M@SC, where M represents the transition metal used (i.e., Cu or Co) and SC the corresponding semiconductors. Noteworthy, the supported M@SCs act as modifying agents enhancing the catalytic activity of the Ni electrodes. For simplicity, the semiconductors TiO_2, Nb_2O_5 and $Nb_3(PO_4)_5$ are denoted as TiO, NbO, and NbP, respectively. M@SC heterostructures were prepared following photochemical deposition of the metal precursors onto the bare SC as previously described (Fig. S1) [33]. Metal loading was determined by ICP-OES as described in the experimental section and shown in Table 1. M@TiO heterostructures bear the lowest metal loadings with 0.89 and 1.22 wt% of Cu and Co, respectively, while M@NbP and M@NbO support higher metal content; suggesting a preferential photodeposition of metals onto Nb-based semiconductors.

The chemical nature and surface composition of the M@SC heterostructures was determined by X-ray Photoelectron Spectroscopy (XPS). HR-XPS spectra of the metals loaded onto the three different SCs are shown in Fig. 1 and Figs. S4−S5. Different Cu species are formed depending on the nature of

Table 1 − Composition of M@SC heterostructures and HR-XPS analysis.

M@SC	[a]M (wt%)	[b]M $2p_{3/2}$ (eV)	[b]M(X)	[b]Nb or Ti $3d_{5/2}$ (eV)
Cu@TiO	0.89	930.1	Cu(I)	458.4
Cu@NbO	4.56	932.8 & 934.9	Cu(I/II)	207.2
Cu@NbP	4.64	932.8 & 934.9	Cu(I/II)	207.6
Co@TiO	1.22	781.1	Co(II)	458.7
Co@NbO	1.70	781.2	Co(II)	207.0
Co@NbP	3.03	781.3	Co(II)	207.3

[a] ICP-OES analysis.
[b] Binding energies obtained respectively from Co 2p, Cu 2p, Nb 3d and Ti 3d regions.
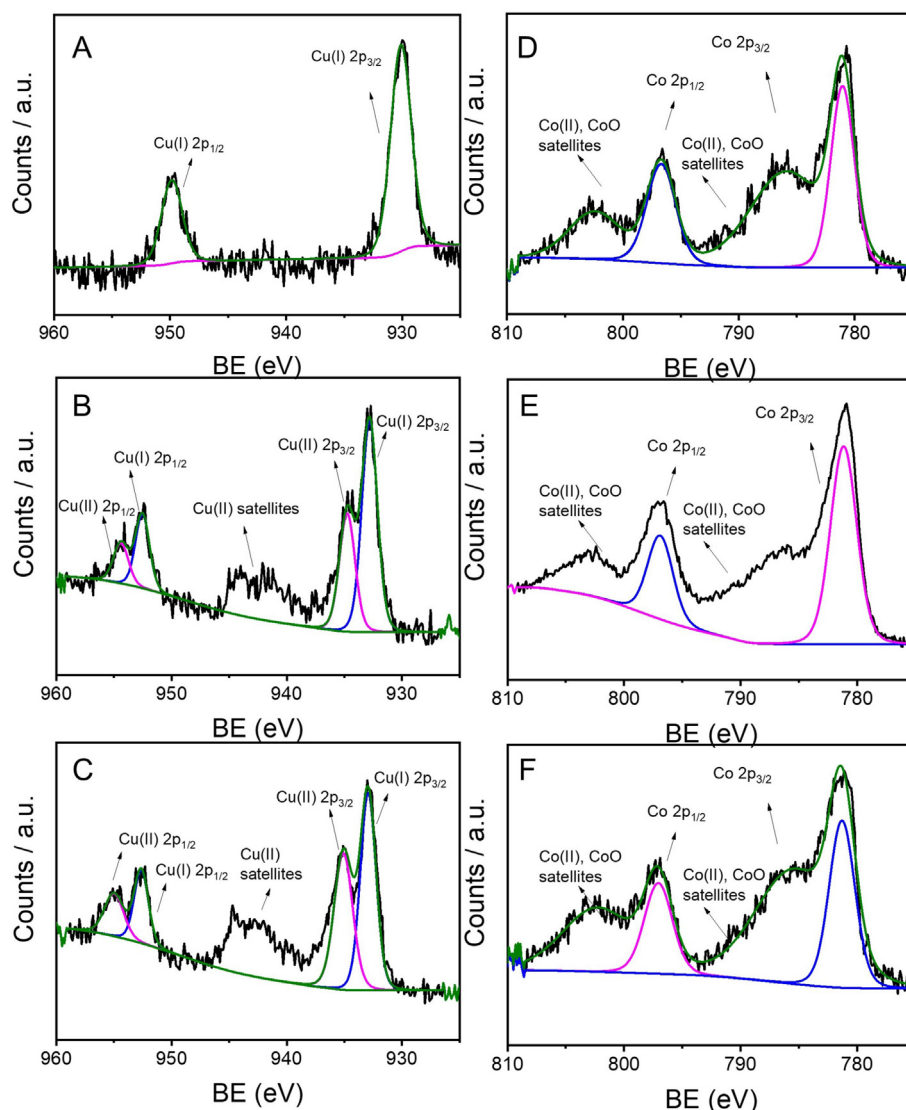
Fig. 1 — Cu 2p and Co 2p HR XPS spectra of A) Cu@TiO, B) Cu@NbO, C) Cu@NbP, D) Co@TiO, E) Co@NbO, and F) Co@NbP.

the SC, in agreement with previous reports [33]. For Cu@NbO and Cu@NbP heterostructures, two Cu $2p_{3/2}$ signals, centered at 932.8 eV and 934.9 eV can be clearly distinguished and are assigned to Cu(I) and Cu(II), respectively. The presence of the Cu(II) satellites further indicate the presence of a mixture of Cu(I)/Cu(II) species. It is worth noting that the amount of Cu(I) species present in Cu@NbO (*ca.* 64%) is slightly higher than in Cu@NbP (*ca.* 54%), which could be related to differences in the surface chemistry of the semiconductor affecting the oxidation state of the metal. In contrast, the Cu 2p HR XPS spectrum for Cu@TiO presents only one Cu $2p_{3/2}$ peak centered at 930.1 eV, which can be attributed to the presence of Cu(I) species —although Cu(0) species cannot be ruled out. Furthermore, no satellite features are found, indicating the absence of Cu (II) species in Cu@TiO. In the case of Co@SC, Co 2p HR XPS spectra show the same features for the three SC, with signals centered at 781.1 eV and 796.9 eV corresponding to Co $2p_{3/2}$ and Co $2p_{1/2}$, respectively. All samples present a spin-orbit coupling ($\Delta_{Co\ 2p\ (1/2-3/2)}$) of 15.7 eV, characteristic of

Co (II) species [39]. Furthermore, satellites features of Co(II) are identified. Therefore, CoO species are likely to be found in the surface of all modified SC.

The optical properties of the materials were measured by means of diffuse reflectance (DR) spectroscopy, Fig. 2. All samples exhibit distinct absorption in the UV region, corresponding to the band-gap absorption of TiO, NbO, and NbP components. After the Cu or Co modification of SC, an increased absorption in the visible region is noticed for all samples. As a result, the optical band-gap energy, obtained from Tauc plots (Fig. S7 and Table 2), slightly decreased in relation to the corresponding SC. Therefore, the absorption edge is shifted for M@SC heterostructures to longer wavelengths, which could facilitate the generation of charge carriers upon visible light absorption. Using the theoretical electronegativity of the SC [40], one could roughly estimate the energy of the band edges [41], which suggest the NbO and NbP families are better suited for formation of H_2. This has been recently demonstrated in literature [14] where nickel catalysts
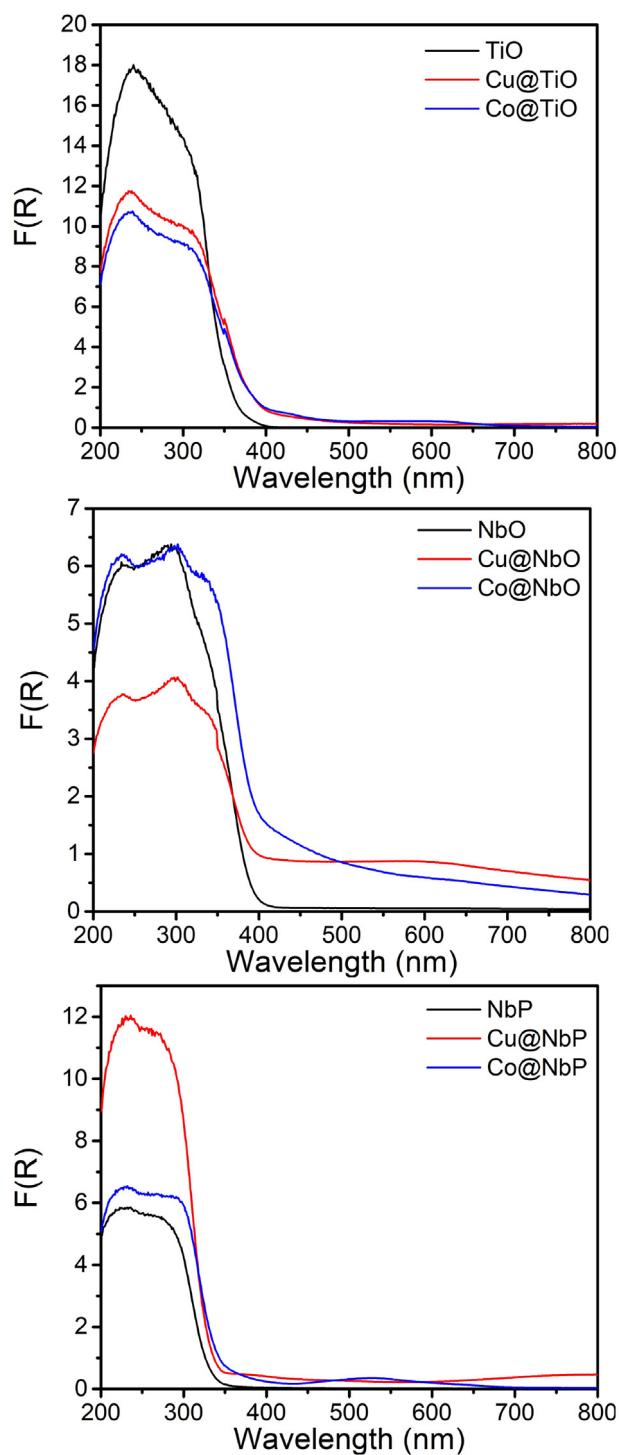
Fig. 2 – Diffuse reflectance spectra of the SC and their corresponding M@SC composites.

Table 2 – Optical band gaps (BG) calculated using Tauc plots (Fig. S7) and valence band (VB) and conduction band (CB) edge energies in eV calculated for each SC and M@SC heterostructures.[a]

M@SC	Optical BG	χ_{SC}[b]	E_{VB}[c]	E_{CB}[c]
[14]TiO	3.19	5.81	2.91	−0.28
Cu@TiO	2.87	5.44	2.38	−0.49
Co@TiO	2.83	5.39	2.30	−0.53
[14]NbO	2.99	6.29	3.29	0.30
Cu@NbO	2.73	6.03	2.89	0.16
Co@NbO	2.74	6.00	2.87	0.13
[14]NbP	3.50	6.68	3.93	0.43
Cu@NbP	3.47	6.59	3.83	0.36
Co@NbP	3.35	6.58	3.76	0.41

[a] Electronegativity of the semiconductors (SC) calculated as the geometric average of the absolute electronegativity of the constituent atoms using the electronegativity of each element from literature [40].
[b] Theoretical Ni Fermi level: 0.85 V vs NHE (Work Function of Ni(111): 5.35 eV [42]).
[c] Calculated as [41,43]: $E_{VB} = \chi_{SC} - E_e + 0.5 E_g$ and $E_{CB} = E_{VB} - E_g$.

achieve high-performance in fuel cells [45] and electrolyzers [46] due to its stability and great ion transport properties [47]. PXRD analysis (obtained from Rietveld refinement using Fullprof software) suggests TiO is composed by a mixture of anatase (A) and rutile (R, (13 ± 4) %), NbO contains orthorombic (O) and monoclinic (M, (24 ± 5)%) crystalline structures, and NbP is amorphous [14]. Also, crystal sizes obtained from the PXRD patterns suggest TiO particles (A: 20 nm and R: 28 nm) are smaller than the NbO particles (O: 50 nm, M: 48 nm). XRD patterns of the prepared electrodes show characteristic reflections of faced centered cubic Ni corresponding to the substrate (See Fig. S6), and the SC preserving their crystalline composition. No reflections of Co or Cu oxides were identified in the diffractograms, potentially due to the low metal loading on each M@SC heterostructure (See Table 1).

Photoelectrochemical characterization of M@SC-Ni electrodes

Cyclic voltammetry

Cyclic voltammograms (CVs) were recorded in the range from −1.5 to 0.1 V (vs. SCE) at a scan rate of 5 mVs^{-1} until stabilization, except for the Co@TiO and Cu@NbP catalyst where a reduced scale (−1.5 to −0.3 V vs. SCE) was used to avoid catalyst electrochemical degradation processes observed at higher potentials. The CVs shown in Fig. 3 were performed in the dark and under UVA-Vis light irradiation (See Figs. S3 and S8) and were used to calculate the corresponding onset potentials (Table 3) for the H$_2$ generation reaction (see video provided within the supplementary materials). Under dark conditions, it appears as if both NbO and NbP decrease the onset potential when comparing with bare Ni electrodes (OP = −1.1 eV), Table S1; whereas TiO slightly increase the onset potential values. Interestingly, the addition of Cu or Co has different impact on the onset potential values depending on the semiconductor. Overall, these values indicate that the smallest overpotential (η) towards hydrogen evolution is obtained for the Co@NbO–Ni electrode (Table S1). This is,

modified with NbO and NbP exhibit higher catalytic activity compared to those modified with TiO, and can be seen in Fig. 3 and Fig. S8.

After the synthesis and characterization of the M@SC, the new electrodes (M@SC-Ni) were prepared by deposition of the M@SC heterostructures onto clean Ni electrodes employing a widely used ink strategy [44], utilizing Nafion as ionomer binder (See Fig. 3A). Nafion has been the preferred choice to
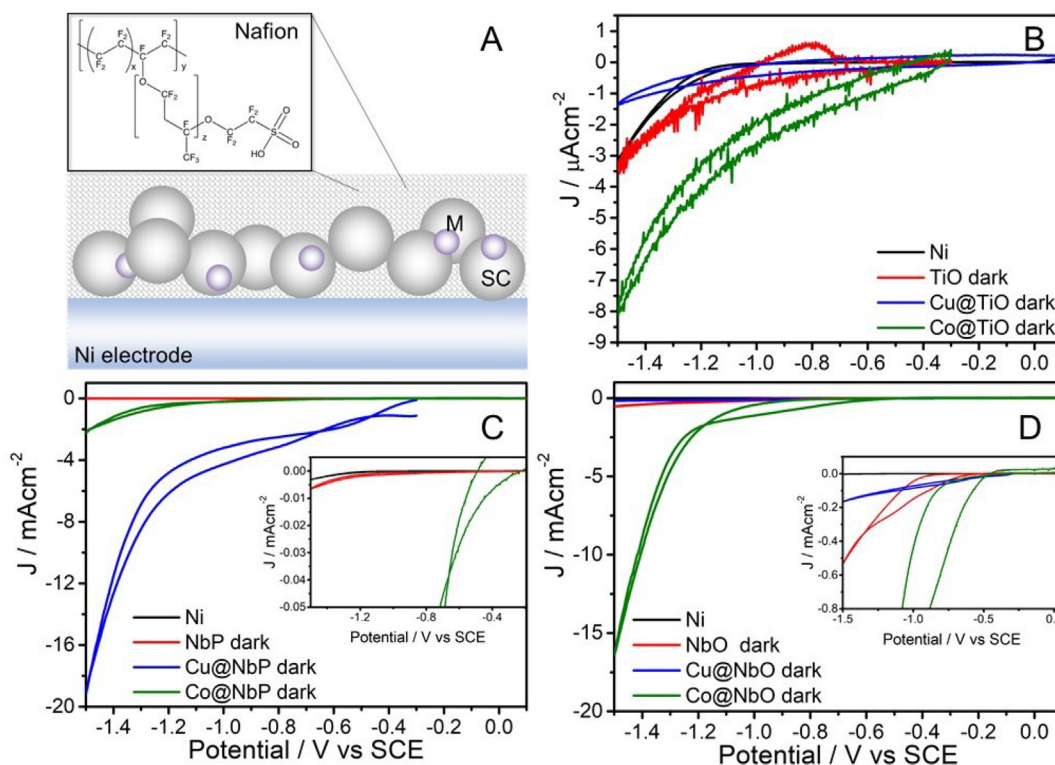
Fig. 3 − (A) Representative diagram of the working electrodes composed of a Ni substrate and the M@SC heterostructures embedded in a Nafion matrix. (B−D) CV obtained for each M@SC-Ni electrocatalyst under dark conditions in a 0.5 M K_2CO_3 solution (pH = 11). Insets: closer look to the onset potential of H_2 formation. Note panel B lower signal-to-noise ratio is due to low current density values detected (y-axis units in μAcm^{-2}). Panel C: CV corresponding to Cu@NbP (blue line) is out of scale and not shown in the inset. (For interpretation of the references to color in this figure legend, the reader is referred to the Web version of this article.)

Table 3 − Exchange current density (j_0), onset potential (OP) and current density (J) obtained at −1.5 V.

	j_0 (μAcm^{-2})	OP (V)		ΔOP (mV)	J ($mAcm^{-2}$)		ΔJ (%)
	Dark	Dark	Light		Dark	Light	
TiO−Ni	<1	−1.12	−1.12	0	3.4×10^{-3}	3.7×10^{-3}	8.8
Cu@TiO−Ni	<1	−1.07	−0.95	120	1.4×10^{-3}	1.9×10^{-3}	35.7
Co@TiO−Ni	<1	−1.03	−1.03	0	8.2×10^{-3}	8.2×10^{-3}	0
NbO−Ni	4	−0.96	−0.96	0	5.2×10^{-1}	5.3×10^{-1}	3.3
Cu@NbO−Ni	3	−1.26	−1.19	70	1.6×10^{-1}	1.8×10^{-1}	11.7
Co@NbO−Ni	80	−0.86	−0.86	0	1.6×10^{1}	1.6×10^{1}	0
NbP−Ni	<1	−1.05	−1.05	0	7.0×10^{-3}	7.0×10^{-3}	0
Cu@NbP−Ni	140	−1.08	−1.04	40	1.9×10^{1}	2.0×10^{1}	4.2
Co@NbP−Ni	12	−1.18	−1.18	0	2.2×10^{0}	2.2×10^{0}	0

considering the starting onset potential for HER at −0.65 V vs SCE at pH = 11.0 (calculated from Nernst equation), Co@N-bO−Ni shows an η = 210 mV.

Supplementary video related to this article can be found at https://doi.org/10.1016/j.ijhydene.2022.03.085

As we have recently reported [14], the onset potential for the H_2 generation from SC-Ni electrodes under dark conditions remains unchanged under UVA/Vis light irradiation (Table 3). In contrast, here we show that the presence of Cu in these M@SC heterostructures changes the onset potential towards more positive values upon irradiation, exhibiting some

photocurrent (Fig. S8 and Table 3). No changes on the onset potential (ΔOP) and current density (ΔJ close to zero) are observed when Cu is replaced by Co. Therefore, only Cu deposited onto the TiO, NbO and NbP increases the charge carrier generation under irradiation. As shown by XPS analysis, Cu(I) species were detected in all samples, suggesting the presence of Cu_2O in the surface of the semiconductor heterostructures. The values in Table 3 indicate the initial composition of the Cu@SC could be related to the current density changes observed upon irradiation, thus, the greatest changes are obtained for Cu@TiO, which only shows XPS signals corresponding to Cu(I) species. Although NbO and NbP present

the same copper loading, Cu@NbO led to higher changes in the current comparing with Cu@NP, in agreement with the slightly higher amount of Cu(I) species found by XPS. Cu_2O is an intrinsic p-type material, presents a suitable conduction band position for water reduction, and a direct band gap of 2.0 eV [48]. Therefore, it is possible that upon UV/Vis irradiation these partly oxidized Cu species can generate photo-excited electrons and holes, driving a shift in the onset potential, and small photocurrents in the composite electrode. Note that no new oxidation peaks were detected for any of the catalysts upon irradiation, although this could be due to the low Cu loading on the M@SC. Further analyses using Bode phase plots suggest these changes are related to HER only in the case of Cu@NbO and Cu@NbP (*vide infra*).

Furthermore, the open circuit potential (OCP) values are indicative of the surface state of the electrode, particularly related to its electronic state and Fermi level [49,50]. In the case of SC-Ni electrodes, the OCP corresponds to the Ni OCP (−0.36 V vs SCE), modified by the presence of the SC hetero-structures [14,50]. It is expected that the addition of a co-catalyst (*e.g.*, Cu or Co) would modify the OCP of the composite. Interestingly, most of the M@SC heterostructures studied here show differences in the OCP values (Table 4). This is, Cu or Co co-catalysts generate significant changes to the OCP values comparing with the corresponding TiO- and NbO−Ni based electrodes. This suggests that the presence of these metals affects the Fermi level of the Ni electrode as suggested by Schottky's theory [27]. The same trend is observed in the case of Cu@NbP−Ni electrodes, whereas the addition of Co does not generate significant changes comparing with the NbP−Ni electrode.

The values of the Tafel slope obtained (See Table S1) for each M@SC-Ni electrode are around −120 mVdec^{-1}, indicating that the Volmer step is the rate-determining step during the HER [51]. In alkaline media, the Volmer step involves the transfer of an electron to a water molecule to yield an adsorbed H atom as a reaction intermediate. Fig. S9 shows the different steps of the reactions that constitutes the general mechanism of the hydrogen generation reaction [52]. In order to gain insights into the electrocatalytic properties of the prepared electrodes, the exchange current density (j_0) for each electrode was compared. Typically, Ni electrodes present an j_0 of about 2 μAcm^{-2} measured in alkaline media [53]. As shown in Table 3 the addition of Co and Cu to the TiO−Ni electrodes does not generate significant increase in the j_0, presenting values lower than 1 μAcm^{-2}. This is in agreement with the low theoretical energy values calculated for the conduction bands in Table 2. Additionally, when analizing the current density data at −1.5 V (vs. SCE) on the CV, values between 1 and 8 μAcm^{-2} are observed for all TiO−Ni electrodes. In contrast, the addition of Cu or Co to NbO−Ni and NbP−Ni electrodes can significantly modify the exchange current density. According to the j_0 and J measured at −1.5 V (vs. SCE), Co@NbO and Cu@NbP present the best performance towards HER in alkaline media. Particularly, the addition of Co to NbO−Ni generates a 20-fold increment in the j_0 values, while Cu addition to NbP−Ni induces a 140-fold increase on j_0 values. The increase catalytic activity might be attributed to several factors, including the modification of the Fermi level. This could be particularly seen in the case of Co@TiO and Co@NbO. In contrast, Co@NbP and Cu@SC do not affect the OCP values in relation to the bare SC. In these cases, other effects could be responsible for their increased catalytic activity; for instance, the presence of potential active sites onto the oxidized Co and Cu species has been recently suggested in literature. Zhang et al. have reported that highly disperse Cu_2O nanoparticles in carbon nanotubes can notably increase the catalytic activity towards HER in alkaline media [54]. Additionally, reports on CoO hybrids, supported on carbon [55] or graphene [56], have shown a distinct catalytic activity towards HER.

Electrochemical impedance spectroscopy (EIS)

To further characterize the (photo)electrocatalytic properties of the prepared electrodes a series of Electrochemical Impedance Spectroscopy (EIS) measurements were performed in the dark and under irradiation. The general equation for calculating EIS parameters for hydrogen generation predicts the formation of two semicircles in the complex plane of Nyquist plots. A low frequency semicircle, with a radius dependent on the over-potential, is related to the HER process; and a high frequency semicircle, with a constant radius, is related to the electrode surface [57]. The low-frequency semicircle radius decreases with lower charge transfer resistance. The impedance spectra can be fitted using the Armstrong and Henderson equivalent circuit (denoted as AHEC) [52,57,58] which allows to consider the roughness of the electrode surface and to analyze the presence of simultaneous processes at different frequencies. AHEC can also account for other processes occurring on the electrode surface, such as photoelectrochemical processes [59,60]. Pure Ni electrodes are typically evaluated in alkaline electrolysis at the following potentials: i) the pure Ni open circuit potential (OCP) reported as −0.36 V, ii) pure Ni HER onset potential reported as −1.1 V, iii) −1.2 V, and iv) −1.4 V (vs.SCE). Therefore, these four electrode potentials were chosen to evaluate the EIS response of the prepared electrodes. Fig. 4 shows the impedance spectra in the complex plane for the different M@SC deposited onto the Ni substrate, measured at 298 K in the dark and under irradiation. Particularly, the figure shows the behavior of the catalysts at −1.2 V (vs. SCE) in the dark and under irradiation. This potential is ideal to explore the catalyst activity as there is enough hydrogen generation and low electrochemical noise —in comparison with that observed at more negative potentials. It can be seen from the Nyquist

Table 4 — Open Circuit Potential (OCP) measured in the dark and under UV/Vis light irradiation.

Catalyst	^{a}OCP (mV)	
	Dark	Light
TiO	−82	−90
Cu@TiO	−126	−127
Co@TiO	−179	−187
NbO	−109	−123
Cu@NbO	−148	−143
Co@NbO	−176	−172
NbP	−148	−143
Cu@NbP	−143	−141
Co@NbP	−148	−147

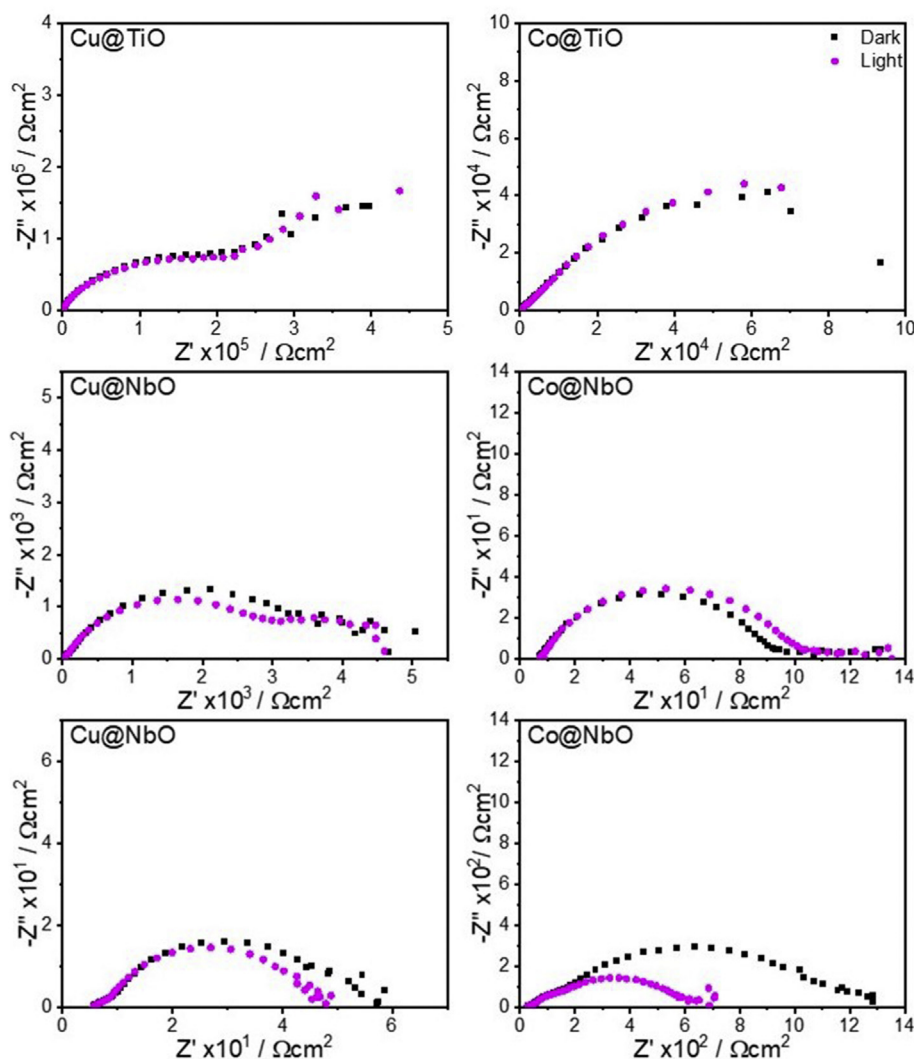^{a} Illumination conditions as described in Fig. S3B.

Fig. 4 — Nyquist plot impedance spectra in the complex plane for the HER for M@SC onto nickel electrodes on 0.5 M K$_2$CO$_3$ at 298 K and −1.2 V (vs. SCE). Measurements were performed in the dark and under UV/Vis light irradiation.

plots that the behaviors are varied and depend on both the semiconductor and the metal present in the catalyst, in agreement with what was found in the cyclic voltammetries. This is, smaller semicircles are found for Co@NbO and Cu@NbP in the dark, consistent with their low overpotentials; whereas slight differences can be seen under irradiation, this was not reflected into higher currents during the voltammetry experiments. In the case of M@TiO—Ni catalysts, no major differences are detected despite the marked increase in current density observed in the cyclic voltammetry experiments. This can be attributed to the overall low current density values observed for M@TiO catalysts and to the occurrence of surface processes unrelated to HER, as discussed below. Additionally, in most of the catalysts a process at high frequencies related to the surface structure of the catalyst is observed (Fig. S10 —zoom in Fig. 4). The second semicircle observed shows dependence with the applied overpotential and is related to the HER [61]. Furthermore, some catalysts show the appearance of a third semicircle at very low frequencies related to the presence of Nafion in the catalytic layer that limits the diffusion of the generated hydrogen [62,63].

To gain a better understanding of the catalysts activity we analysed the Bode phase plots (i.e., phase shift vs. frequency plots, Fig. S11). Similar to what is found in the Nyquist plots, Bode phase plots present two phase shift maxima corresponding to the HER process (low frequency) and the surface processes (high frequency). When an electrode is subjected to a gas evolving reaction —e.g., HER —the phase shift angle maximum (at low frequency) is displaced to higher frequencies and becomes less significant at higher overpotentials. This process is associated with an increased electrode surface coverage generated by formation of bubbles that block the exposed surface [64]. Thus, the electrodes with higher HER efficiency exhibit this type of behavior. Fig. S11 shows that M@TiO—Ni catalysts have almost negligible changes as the overpotential increases, suggesting that although electrochemical processes are observed during cyclic voltammetry, the HER might be incipient and other surface processes (such as reduction of metal oxides) are predominant. Thus, it is possible that the increase current observed for Cu@TiO—Ni under irradiation is due to processes other than HER. A similar behaviour can be seen for

Cu@NbO–Ni catalyst; although this catalyst shows a higher catalytic activity comparing with M@TiO–Ni catalysts. In contrast, Co@NbO–Ni catalyst shows a marked response to higher potentials, similar to that expected during HER, and in agreement with the response observed by cyclic voltammetry. In the case of the M@NbP–Ni catalysts a correlation between the dependence of the phase shift maximum with the overpotential is also observed. In particular, Cu@NbP–Ni catalyst shows a higher response towards hydrogen generation (low frequency maximum) than in the case of Co@NbP–Ni (see arrows in Fig. S11). Additionally, the phase shift angle maximum at high frequencies (related to the surface response) is more predominant for the Co@NbP–Ni catalyst. On the other hand, small fluctuations in the maximum phase shift are observed when applying light mainly at the onset potential. This fluctuation could be due to the appearance of new electrochemical processes upon irradiation. This is supported by the values obtained from the A & E equivalent circuit fitting model —where increase in the R_{ct} values does not affect the current density. Table 5 shows R_{ct} value is particularly increased for Co@NbP–Ni catalyst while j value decrease is negligible (Fig. S8). Thus, the appearance of a new process related to surface irradiation can lead to errors in the fit performed with an equivalent circuit that only considers two processes. The phase shift increase could be due to the irradiation effect, which becomes noticeable at lower external potentials, while at potentials where the hydrogen evolution reaction is being externally forced, small reductions of the charge transfer resistance (R_{ct}) are observed when irradiating with UV–Vis light, as in the case of Cu@SC-Ni catalysts (See Table 5). Considering that the phase shift peak is related to charge transfer, this supports a favourable charge transfer upon irradiation [65]. The complete electrochemical impedance parameters obtained by fitting the experimental data with the Armstrong & Henderson equivalent circuit is presented in Table S2.

Kelvin probe force microscopy analysis

Kelvin probe force microscopy (KPFM) was used to characterize the impact of the Co and Cu deposition on the surface potential properties of the electrodes in the dark or under visible light irradiation (Fig. S3). In Fig. 5 a mapping of surface potential of representative electrodes under dark conditions can be found. Clearly, the deposition of the M@SC heterostructures onto the Ni substrate modifies the surface potential of the electrodes. Although the absolute work functions values are difficult to obtain under ambient conditions [66], KPFM can measure a contact potential difference (CPD) between the sample surface and the tip (V_{CPD}). The V_{CPD} of the M@SC-Ni electrodes could be used to estimate the work function from different electrodes Fig. S12) considering the Ni electrode V_{CPD} as a reference, corresponding to a work
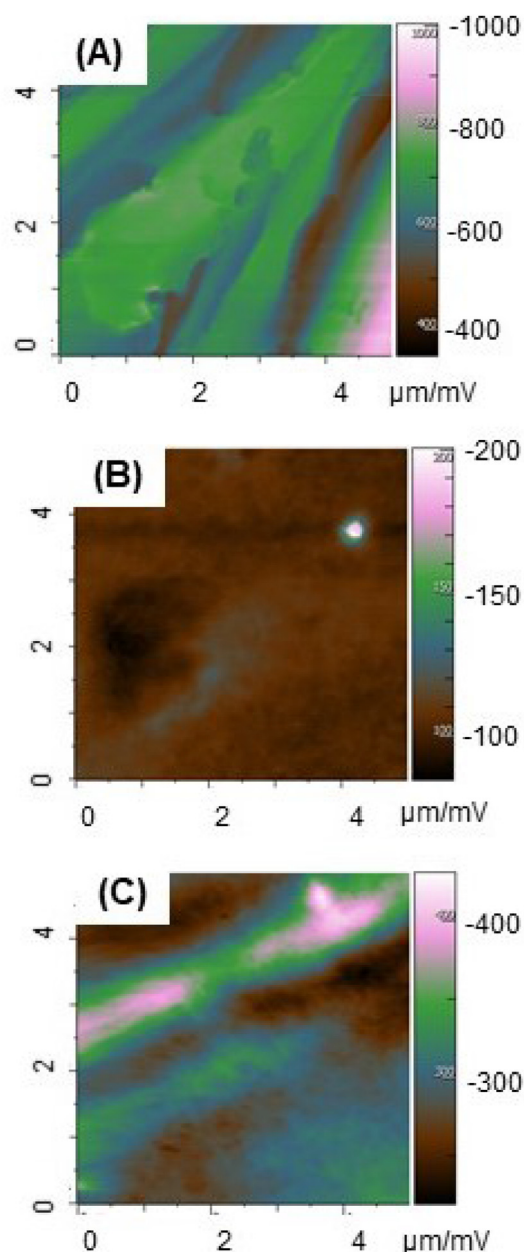

Fig. 5 – Mapping representing contrast in surface potential of A) Ni, B) Cu@NbO–Ni, C) Co@NbO–Ni electrodes.

function value equals to 5.35 eV (See Table 6) [67]. The analyses suggest that Cu or Co co-catalysts change the work function values of the corresponding M@SC-Ni electrodes. While V_{CPD} values for M@TiO–Ni electrodes are strongly reduced in the presence of Cu or Co, the opposite effect is found on M@NbO- and M@NbP–Ni electrodes —affecting more NbO-based electrodes.

Table 5 – Charge transfer resistance obtained using the AHEC model for all the catalysts under dark and irradiation.

		TiO		NbP		NbO	
		Dark	Light	Dark	Light	Dark	Light
Co	$R_{ct}/\Omega.cm^2$	19422.0	19983.0	353.3	430.7	11.9	12.4
Cu	$R_{ct}/\Omega.cm^2$	132930.0	799.0	6.5	5.0	409.3	367.0

Table 6 – Contact Potential Difference V_{CPD} and theoretical work function (φ).

Catalyst	$^a V_{CPD}$ (mV)		φ (eV)	
	Dark	Light	Dark	Light
TiO	774.1	769.8	5.53	5.53
Cu@TiO	178.7	230.7	4.94	4.99
Co@TiO	−73.9	−73.1	4.68	4.68
NbO	9.9	9.8	4.77	4.77
Cu@NbO	105.3	110.0	4.86	4.87
Co@NbO	301.3	303.9	5.06	5.06
NbP	133.7	136.4	4.89	4.89
Cu@NbP	185.6	190.0	4.94	4.95
Co@NbP	242.0	252.4	5.00	5.01

[a] Determined by KPFM, illumination conditions described in Fig. S3C. V_{CPD} values for Ni plate were 586.9 mV and 583.0 mV in the dark and under illumination respectively.

Figs. S13–S15 show the CPD images for all materials in the dark and under irradiation. From the potentials obtained, Table 6 was made. Using the information from Table 6, the work function of each electrode can be estimated. The energy diagram shown in Fig. S12 takes into consideration the Fermi level ($E_f = -\varphi$) of the prepared electrodes and bare Ni. The Fermi level of modified electrodes, estimated from KPFM measurements, is shifted towards more negative potentials compared to Ni, which thermodynamically favours the HER. Although the surface energy band diagram may change drastically upon contact with the electrolyte, the estimated values obtained from KPFM and OCP studies indicate that the deposition of Cu and Co onto the SC can alter the surface potential properties of the modified Ni electrocatalyts. On the other hand, under stationary irradiation using visible light (no direct excitation of the SC), Cu@TiO heterostructures presented the highest shift in the V_{CPD} values, indicating a surface potential rearrangement upon irradiation, in agreement with the higher response found in cyclic voltammetry.

Conclusions

We have presented a strategy for the preparation of hybrid Nickel electrodes with semiconductor heterostructures using Nafion as a binder. As previously showed, the presence of Nb-based semiconductors (NbO and NbP) can increase the production of hydrogen drasticaly. Here we showed that deposition of Co or Cu oxides onto these Nb-based semiconductors can increase the current density even more, suggesting semiconductor heterostructures can boost the HER efficiency of Nickel composite electrodes. Remarkably, the Ni composite electrodes composed by Cu and Nb semiconductor heterostructures (Cu@NbSC–Ni) show enhanced activity under photoelectrochemical conditions, even when the corresponding SC-Ni electrode is unaltered under the same irradiation conditions. Nevertheless, EIS studies suggest only the enhanced activity of Cu@NbP–Ni electrodes is related to hydrogen generation, whereas other processes, possibly surface processes, could dominate the increase photocurrent seen for NbO and TiO counterparts. In this

sense, it is possible that the amorphous nature of NbP contributes to more favourable Cu-SC surface interactions. Studying differences in the surface and electronic interactions between Cu and the two NbSC could give more insights into this apparent better performance. Based on the Schottky barrier theory, the inclusion of a third metal such as Co or Cu could generate an electron flow that enhances the interaction between the nickel and the oxides improving the response of the catalytic activity of NbSC–Ni heterojunctions. This work shows small amounts of earth-abundant co-catalysts can greatly affect the activity of Nb-based Ni composite electrodes significantly improving hydrogen generation processes under laboratory conditions. This study constitutes the first approach to use this type of materials for hydrogen photoelectrogeneration. Noteworthy, the materials used can be synthesised in large scale —TiO_2 is widely used in different industries and niobium semiconductors have recently attracted attention for potential uses in batteries [68]. Yet, the use of these materials as modifying agents for photocathodes has been little explored in literature. Overall, the materials have interesting properties to be considered for applications in photoelectrochemical generation of hydrogen and open an opportunity for the use of new materials in the production of green hydrogen.

Declaration of competing interest

The authors declare that they have no known competing financial interests or personal relationships that could have appeared to influence the work reported in this paper.

Acknowledgements

Appendix A Supplementary data

Supplementary data to this article can be found online at https://doi.org/10.1016/j.ijhydene.2022.03.085.

REFERENCES

[1] Fujishima A, Honda K. Electrochemical photolysis of water at a semiconductor electrode. Nature 1972;238(5358):37–8. https://doi.org/10.1038/238037a0.

[2] Caglayan DG, Heinrichs HU, Robinius M, Stolten D. Robust design of a future 100% renewable european energy supply

system with hydrogen infrastructure. Int J Hydrogen Energy 2021;46(57):29376–90. https://doi.org/10.1016/j.ijhydene.2020.12.197.

[3] Hernandez DD, Gençer E. Techno-economic analysis of balancing California's power system on a seasonal basis: hydrogen vs. lithium-ion batteries. Appl Energy 2021;300:117314. https://doi.org/10.1016/j.apenergy.2021.117314.

[4] Sasanpour S, Cao K-K, Gils HC, Jochem P. Strategic policy targets and the contribution of hydrogen in a 100% renewable european power system. Energy Rep 2021;7:4595–608. https://doi.org/10.1016/j.egyr.2021.07.005.

[5] Ding Q, Gou L, Wei D, Xu D, Fan W, Shi W. Metal-organic framework derived Co_3O_4/TiO_2 heterostructure nanoarrays for promote photoelectrochemical water splitting. Int J Hydrogen Energy 2021;46(49):24965–76. https://doi.org/10.1016/j.ijhydene.2021.05.065.

[6] Luna NS, Correa-Perelmuter G, Lacconi GI, Diaz LA, Franceschini EA. In operando activation of alkaline electrolyzer by ruthenium spontaneous deposition. J Solid State Electrochem 2021;25(3):1019–27. https://doi.org/10.1007/s10008-020-04857-y.

[7] Gong M, Wang D-Y, Chen C-C, Hwang B-J, Dai H. A mini review on nickel-based electrocatalysts for alkaline hydrogen evolution reaction. Nano Res 2016;9(1):28–46. https://doi.org/10.1007/s12274-015-0965-x.

[8] Schiller G, Henne R, Mohr P, Peinecke V. High performance electrodes for an advanced intermittently operated 10-kw alkaline water electrolyzer. Int J Hydrogen Energy 1998;23(9):761–5. https://doi.org/10.1016/S0360-3199(97)00122-5.

[9] Martínez W, Fernández A, Cano U, Sandoval J A. Synthesis of nickel-based skeletal catalyst for an alkaline electrolyzer. Int J Hydrogen Energy 2010;35(16):8457–62. https://doi.org/10.1016/j.ijhydene.2010.04.109.

[10] Schalenbach M, Kasian O, Mayrhofer KJ. An alkaline water electrolyzer with nickel electrodes enables efficient high current density operation. Int J Hydrogen Energy 2018;43(27):11932–8. https://doi.org/10.1016/j.ijhydene.2018.04.219.

[11] Xie T, Zhao H, Lv Z, Xie G, He Y. A highly active composite electrocatalyst Ni–Fe–P–Nb_2O_5/NF for overall water splitting. Int J Hydrogen Energy 2021;46(1):581–8. https://doi.org/10.1016/j.ijhydene.2020.09.244.

[12] Hall DS, Lockwood DJ, Bock C, MacDougall BR. Nickel hydroxides and related materials: a review of their structures, synthesis and properties. Proc Math Phys Eng Sci 2015;471(2174):20140792. https://doi.org/10.1098/rspa.2014.0792.

[13] Hall DS, Lockwood DJ, Poirier S, Bock C, MacDougall BR. Applications of in situ Raman spectroscopy for identifying nickel hydroxide materials and surface layers during chemical aging. ACS Appl Mater Interfaces 2014;6(5):3141–9. https://doi.org/10.1021/am405419k.

[14] Franceschini EA, Hainer A, Lanterna AE. Niobium-based semiconductor electrodes for hydrogen evolution reaction. Int J Hydrogen Energy 2019;44(60):31940–8. https://doi.org/10.1016/j.ijhydene.2019.10.101.

[15] Gómez MJ, Benavente-Llorente V, Hainer A, Lacconi GI, Scaiano JC, Franceschini EA, Lanterna AE. Evaluation of different Ni–semiconductor composites as electrodes for enhanced hydrogen evolution reaction. Sustain Energy Fuels 2020;4:3963–70. https://doi.org/10.1039/D0SE00634C.

[16] Zelcer A, Franceschini EA, Lombardo MV, Lanterna AE, Soler-Illia GJAA. A general method to produce mesoporous oxide spherical particles through an aerosol method from aqueous solutions. J Sol Gel Sci Technol 2020;94(1):195–204. https://doi.org/10.1007/s10971-019-05175-0.

[17] Lin F, Boettcher SW. Advanced photoelectrochemical characterization: principles and applications of dual-Working-electrode photoelectrochemistry. Cham: Springer International Publishing; 2016. p. 323–51. https://doi.org/10.1007/978-3-319-29641-8_7. Ch. 7.

[18] Berardi S, Kopula Kesavan J, Amidani L, Meloni EM, Marelli M, Boscherini F, Caramori S, Pasquini L. Better together: ilmenite/hematite junctions for photoelectrochemical water oxidation. ACS Appl Mater Interfaces 2020;12(42):47435–46. https://doi.org/10.1021/acsami.0c12275.

[19] Nellist MR, Laskowski FAL, Lin F, Mills TJ, Boettcher SW. Semiconductor–electrocatalyst interfaces: theory, experiment, and applications in photoelectrochemical water splitting. Acc Chem Res 2016;49(4):733–40. https://doi.org/10.1021/acs.accounts.6b00001.

[20] Azadi G, Bagheri R, Bikas R, Mousazade Y, Cui J, Song Z, Kinzhybalo V, Shen J-R, Allakhverdiev SI, Najafpour MM. A transparent electrode with water-oxidizing activity. Int J Hydrogen Energy 2018;43(51):22896–904. https://doi.org/10.1016/j.ijhydene.2018.10.146.

[21] Mehrabani S, Bikas R, Zand Z, Mousazade Y, Allakhverdiev SI, Najafpour MM. Water splitting by a pentanuclear iron complex. Int J Hydrogen Energy 2020;45(35):17434–43. https://doi.org/10.1016/j.ijhydene.2020.04.249.

[22] Qiu P, Zhang Y, Cheng G. Precursor self-derived Cu@TiO_2 hybrid Schottky junction for enhanced solar-to-hydrogen evolution. Int J Hydrogen Energy 2022;47(19):10628–37. https://doi.org/10.1016/j.ijhydene.2022.01.113.

[23] Fu Z, Ma X, Xia B, Hu X, Fan J, Liu E. Efficient photocatalytic H_2 evolution over Cu and Cu_3P co-modified TiO_2 nanosheet. Int J Hydrogen Energy 2021;46(37):19373–84. https://doi.org/10.1016/j.ijhydene.2021.03.089.

[24] Tryk D, Fujishima A, Honda K. Recent topics in photoelectrochemistry: achievements and future prospects. Electrochim Acta 2000;45(15):2363–76. https://doi.org/10.1016/S0013-4686(00)00337-6.

[25] Tung RT. The physics and chemistry of the Schottky barrier height. Appl Phys Rev 2014;1(1):011304. https://doi.org/10.1063/1.4858400.

[26] Li H, Shi Y, Shang H, Wang W, Lu J, Zakharov AA, Hultman L, Uhrberg RIG, Syväjärvi M, Yakimova R, Zhang L, Sun J. Atomic-scale tuning of graphene/cubic SiC Schottky junction for stable low-bias photoelectrochemical solar-to-fuel conversion. ACS Nano 2020;14(4):4905–15. https://doi.org/10.1021/acsnano.0c00986.

[27] Zhang W, Wang B, Hao C, Liang Y, Shi H, Ao L, Wang W. Au/Cu_2O Schottky contact heterostructures with enhanced photocatalytic activity in dye decomposition and photoelectrochemical water splitting under visible light irradiation. J Alloys Compd 2016;684:445–52. https://doi.org/10.1016/j.jallcom.2016.05.192.

[28] Zhang N, Qi M-Y, Yuan L, Fu X, Tang Z-R, Gong J, Xu Y-J. Broadband light harvesting and unidirectional electron flow for efficient electron accumulation for hydrogen generation. Angew Chem Int Ed 2019;58(29):10003–7. https://doi.org/10.1002/anie.201905981. arXiv:https://onlinelibrary.wiley.com/doi/pdf/10.1002/anie.201905981.

[29] Zhang Q, Zhai B, Lin Z, Zhao X, Diao P. CuO/$CuBi_2O_4$ bilayered heterojunction as an efficient photocathode for photoelectrochemical hydrogen evolution reaction. Int J Hydrogen Energy 2021;46(21):11607–20. https://doi.org/10.1016/j.ijhydene.2021.01.050.

[30] Marathey P, Patel B, Khanna S, Vanpariya A, Ray A. Photoelectrochemical characteristics of electrodeposited cuprous oxide with protective over layers for hydrogen evolution reactions. Int J Hydrogen Energy

2021;46(30):16431–9. https://doi.org/10.1016/j.ijhydene.2020.07.271.

[31] Patel PP, Velikokhatnyi OI, Ghadge SD, Hanumantha PJ, Datta MK, Kuruba R, Gattu B, Shanthi PM, Kumta PN. Electrochemically active and robust cobalt doped copper phosphosulfide electro-catalysts for hydrogen evolution reaction in electrolytic and photoelectrochemical water splitting. Int J Hydrogen Energy 2018;43(16):7855–71. https://doi.org/10.1016/j.ijhydene.2018.02.147.

[32] Rodríguez-Carvajal J. Recent advances in magnetic structure determination by neutron powder diffraction. Phys B Condens Matter 1993;192(1):55–69. https://doi.org/10.1016/0921-4526(93)90108-I.

[33] Wang B, Durantini J, Nie J, Lanterna AE, Scaiano JC. Heterogeneous photocatalytic click chemistry. J Am Chem Soc 2016;138(40):13127–30. https://doi.org/10.1021/jacs.6b06922.

[34] Wang B, Duke K, Scaiano JC, Lanterna AE. Cobalt-molybdenum co-catalyst for heterogeneous photocatalytic H-mediated transformations. J Catal 2019;379:33–8. https://doi.org/10.1016/j.jcat.2019.09.015.

[35] Morgan RD, Haan JL, Masel RI. Effects of nafion loading in anode catalyst inks on the miniature direct formic acid fuel cell. J Power Sources 2010;195(19):6405–10. https://doi.org/10.1016/j.jpowsour.2010.04.001.

[36] Lopez-Haro M, Guétaz L, Printemps T, Morin A, Escribano S, Jouneau PH, Bayle-Guillemaud P, Chandezon F, Gebel G. Three-dimensional analysis of nafion layers in fuel cell electrodes. Nat Commun 2014;5(1):5229. https://doi.org/10.1038/ncomms6229.

[37] Franceschini EA, Lacconi GI. Synthesis and performance of nickel/reduced graphene oxide hybrid for hydrogen evolution reaction. Electrocatalysis 2018;9(1):47–58. https://doi.org/10.1007/s12678-017-0415-5.

[38] Gómez MJ, Loiácono A, Pérez LA, Franceschini EA, Lacconi GI. Highly efficient hybrid Ni/nitrogenated graphene electrocatalysts for hydrogen evolution reaction. ACS Omega 2019;4(1):2206–16. https://doi.org/10.1021/acsomega.8b02895.

[39] Xiao G, Han Y, Jing F, Chen M, Chen S, Zhao F, Xiao S, Zhang Y, Li J, Hong J. Preparation of highly dispersed Nb_2O_5 supported cobalt-based catalysts for the Fischer-Tropsch synthesis. Ind Eng Chem Res 2020;59(39):17315–27. https://doi.org/10.1021/acs.iecr.0c01248.

[40] Pearson RG. Absolute electronegativity and hardness: application to inorganic chemistry. Inorg Chem 1988;27(4):734–40. https://doi.org/10.1002/chin.198821002.

[41] Tian N, Huang H, He Y, Guo Y, Zhang T, Zhang Y. Mediator-free direct Z-scheme photocatalytic system: $BiVO_4/g-C_3N_4$ organic–inorganic hybrid photocatalyst with highly efficient visible-light-induced photocatalytic activity. Dalton Trans 2015;44:4297–307. https://doi.org/10.1039/C4DT03905J.

[42] Rumble J. CRC handbook of chemistry and physics. Boca Raton, FL: CRC Press; 2018.

[43] Huang Q-Z, Wang J-C, Wang P-P, Yao H-C, Li Z-J. In-situ growth of mesoporous Nb_2O_5 microspheres on g–C_3N_4 nanosheets for enhanced photocatalytic H_2 evolution under visible light irradiation. Int J Hydrogen Energy 2017;42(10):6683–94. https://doi.org/10.1016/j.ijhydene.2017.02.052.

[44] Jiang G, Yu H, Li Y, Yao D, Chi J, Sun S, Shao Z. Low-loading and highly stable membrane electrode based on an Ir@WO x NR ordered array for PEM water electrolysis. ACS Appl Mater Interfaces 2021;13(13):15073–82. https://doi.org/10.1021/acsami.0c20791.

[45] Li Y, Van Cleve T, Sun R, Gawas R, Wang G, Tang M, Elabd YA, Snyder J, Neyerlin KC. Modifying the electrocatalyst–ionomer interface via sulfonated poly(ionic liquid) block copolymers to enable high-performance polymer electrolyte fuel cells. ACS Energy Lett 2020;5(6):1726–31. https://doi.org/10.1021/acsenergylett.0c00532. arXiv:https://doi.org/10.1021/acsenergylett.0c00532.

[46] Mo J, Stefanov BI, Lau TH, Chen T, Wu S, Wang Z, Gong XQ, Wilkinson I, Schmid G, Tsang SCE. Superior performance of Ag over Pt for hydrogen evolution reaction in water electrolysis under high overpotentials. ACS Appl Energy Mater 2019;2(2):1221–8. https://doi.org/10.1021/acsaem.8b01777.

[47] Diat O, Gebel G. Proton channels. Nat Mater 2008;7(1):13–4. https://doi.org/10.1038/nmat2091.

[48] John S, Roy SC. CuO/Cu_2O nanoflake/nanowire heterostructure photocathode with enhanced surface area for photoelectrochemical solar energy conversion. Appl Surf Sci 2020;509:144703. https://doi.org/10.1016/j.apsusc.2019.144703.

[49] Caprioglio P, Stolterfoht M, Wolff CM, Unold T, Rech B, Albrecht S, Neher D. On the relation between the open-circuit voltage and quasi-Fermi level splitting in efficient perovskite solar cells. Adv Energy Mater 2019;9(33):1901631. https://doi.org/10.1002/aenm.201901631. arXiv:https://onlinelibrary.wiley.com/doi/pdf/10.1002/aenm.201901631.

[50] Zhang XG. Basic theories of semiconductor electrochemistry. Boston, MA: Springer US; 2001. p. 1–43. https://doi.org/10.1007/0-306-47921-4_1. Ch. 1.

[51] Kreysa G, Hakansson B, Ekdunge P. Kinetic and thermodynamic analysis of hydrogen evolution at nickel electrodes. Electrochim Acta 1988;33(10):1351–7. https://doi.org/10.1016/0013-4686(88)80125-7.

[52] Franceschini EA, Gomez MJ, Lacconi GI. One step synthesis of high efficiency nickel/mesoporous TiO_2 hybrid catalyst for hydrogen evolution reaction. J Energy Chem 2019;29:79–87. https://doi.org/10.1016/j.jechem.2018.02.005.

[53] Loiácono A, Gómez MJ, Franceschini EA, Lacconi GI. Enhanced hydrogen evolution activity of Ni[MoS_2] hybrids in alkaline electrolyte. Electrocatalysis 2020;11(3):309–16. https://doi.org/10.1007/s12678-020-00588-w.

[54] Zhang Y, Yan Z, Zhang M, Tan Y, Jia S, Liu A. Green electroless plating of cuprous oxide nanoparticles onto carbon nanotubes as efficient electrocatalysts for hydrogen evolution reaction. Appl Surf Sci 2021;548:149218. https://doi.org/10.1016/j.apsusc.2021.149218.

[55] Li X, Niu Z, Jiang J, Ai L. Cobalt nanoparticles embedded in porous N-rich carbon as an efficient bifunctional electrocatalyst for water splitting. J Mater Chem 2016;4(9):3204–9. https://doi.org/10.1039/c6ta00223d.

[56] Ullah N, Xie M, Chen L, Yaseen W, Zhao W, Yang S, Xu Y, Xie J. Novel 3D graphene ornamented with CoO nanoparticles as an efficient bifunctional electrocatalyst for oxygen and hydrogen evolution reactions. Mater Chem Phys 2021;261:124237. https://doi.org/10.1016/j.matchemphys.2021.124237.

[57] Hitz C, Lasia A. Experimental study and modeling of impedance of the her on porous ni electrodes. J Electroanal Chem 2001;500(1–2):213–22. https://doi.org/10.1016/S0022-0728(00)00317-X.

[58] Gomez MJ, Franceschini EA, Lacconi GI. Ni and Ni_xCo_y alloys electrodeposited on stainless steel AISI 316L for hydrogen evolution reaction. Electrocatalysis 2018;9(4):459–70. https://doi.org/10.1007/s12678-018-0463-5.

[59] Lopes T, Andrade L, Ribeiro HA, Mendes A. Characterization of photoelectrochemical cells for water splitting by electrochemical impedance spectroscopy. Int J Hydrogen Energy 2010;35(20):11601–8. https://doi.org/10.1016/j.ijhydene.2010.04.001.

[60] Hosseini MG, Sefidi PY, Aydin Z, Kinayyigit S. Toward enhancing the photoelectrochemical water splitting efficiency of organic acid doped polyaniline-WO_3 photoanode by photo-assisted electrochemically reduced graphene oxide. Electrochim Acta 2020;333:135475. https://doi.org/10.1016/j.electacta.2019.135475.

[61] Lasia A. Nature of the two semi-circles observed on the complex plane plots on porous electrodes in the presence of a concentration gradient. J Electroanal Chem 2001;500(1):30—5. https://doi.org/10.1016/S0022-0728(00)00361-2.

[62] Latorrata S, Pelosato R, Gallo Stampino P, Cristiani C, Dotelli G. Use of electrochemical impedance spectroscopy for the evaluation of performance of pem fuel cells based on carbon cloth gas diffusion electrodes. Int. J Spectrosc 2018;2018:3254375. https://doi.org/10.1155/2018/3254375.

[63] M. Grandi, K. Mayer, M. Gatalo, G. Kapun, F. Ruiz-Zepeda, B. Marius, M. Gaberšček, V. Hacker, The influence catalyst layer thickness on resistance contributions of pemfc determined by electrochemical impedance spectroscopy, Energies 14 (21). doi:10.3390/en14217299.

[64] Lyons M, Brandon M. The significance of electrochemical impedance spectra recorded during active oxygen evolution for oxide covered Ni, Co and Fe electrodes in alkaline solution. J Electroanal Chem 2009;631(1):62—70. https://doi.org/10.1016/j.jelechem.2009.03.019.

[65] da Silva Pelissari MR, Scalvi LVA, Neto VSL, Dall'Antonia LH. Evaluation of the heterostructure ITO/$BiVO_4$ under blue monochromatic light irradiation for photoelectrochemical application. J Mater Sci Mater Electron 2020;31(4):2833—44. https://doi.org/10.1007/s10854-019-02827-3.

[66] Shearer MJ, Li MY, Li LJ, Jin S, Hamers RJ. Nanoscale surface photovoltage mapping of 2D materials and heterostructures by illuminated Kelvin probe force microscopy. J Phys Chem C 2018;122(25):13564—71. https://doi.org/10.1021/acs.jpcc.7b12579.

[67] Jayanthi S, Muthu DVS, Jayaraman N, Sampath S, Sood AK. Semiconducting conjugated microporous polymer: an electrode material for photoelectrochemical water splitting and oxygen reduction. ChemistrySelect 2017;2(16):4522—32. https://doi.org/10.1002/slct.201700505.

[68] Ding H, Song Z, Zhang H, Zhang H, Li X. Niobium-based oxide anodes toward fast and safe energy storage: a review. Materials Today Nano 2020;11:100082. https://doi.org/10.1016/j.mtnano.2020.100082.